Critical hydrogen concentration for crack propagation in a CrMo steel: targeted experiments for accurate numerical modelling

Luis Borja Peral [1], Inés Fernández-Pariente [2], Chiara Colombo [3]*

[1] Department of Civil Engineering, Structural Integrity Research Group, Higher Polytechnic School, University of Burgos, Avenida de Cantabria s/n, 09006 Burgos, Spain
[2] University of Oviedo, Campus of Gijón, East building, 33203 Gijón, Spain
[3] Politecnico di Milano, Department of Mechanical Engineering, Via La Masa 1, 20156 Milano, Italy

*Corresponding author: chiara.colombo@polimi.it

Abstract

This study focuses on CrMo steel experiencing decohesion mechanism in presence of hydrogen. Tensile, permeation and toughness experimental tests are performed to obtain all the inputs for the numerical simulations of a propagating crack in a C(T) specimen. The used finite element framework is based on the cohesive zone modelling. Given the tailored inputs, these models are accurate and allow for estimating the hydrogen concentrations in the lattice and the reversible traps, and following their redistribution along the ligament during the time. From the obtained results, we could quantify that a decrease of two orders of magnitude in the test speed reduces the critical hydrogen concentration at the crack tip, necessary to activate the failure of the first cohesive element and therefore the propagation, from 0.994 to 0.784 wppm, that is -21%.

Keywords

Hydrogen embrittlement; Hydrogen diffusion; CrMo steel; Crack tip; Cohesive Zone Modelling.

1 Introduction

The exposure of metallic alloys to environments where hydrogen is present and can enter into the lattice in its atomic form can result in the hydrogen embrittlement phenomenon. Hydrogen access to the steel structure can occur during the material production, being present before load application, or during the exercise as a result of environmental exposure, e.g. cathodic electrochemical reactions [1]. However, independently of its source, when atomic hydrogen is present in a component, it can be deleterious for its structural assessment, inducing a drop in mechanical performance, especially in terms of fracture toughness [2–5].

The literature used some experimental approaches to understand the active mechanisms inducing hydrogen embrittlement, focusing the attention on fracture mechanics tests, i.e. fracture toughness [6–8] and fatigue crack growth tests [9–13]. However, the identification of single or multiple active mechanisms is still debated, because each steel behaves differently and can be more or less prone to hydrogen embrittlement based on its microstructure and alloy elements, as well as on the type of applied load. In parallel to the experimental testing, also some numerical models at the macroscale have been developed to support the experimental observations [14–17]. Indeed, they have been used as powerful tools to estimate many field quantitates which are difficult or even impossible to measure experimentally, such as hydrogen concentrations near a crack tip. The experimental measurement of hydrogen is quite difficult and limited to average values over a sample of unloaded material [18]. This means that it is still very challenging from the experimental viewpoint to measure the hydrogen concentrations and, in particular, the effective critical value able to induce crack propagation under a given loading condition.

The choice of the most suitable numerical model needs some comments. Indeed, at least two factors must be taken into account: the framework and the inputs. The first point is the selection of the numerical framework and driving equations, which depend in turn on the main mechanism/mechanisms active during the crack initiation and propagation. Indeed, different numerical approaches have been developed, considering for instance the hydrogen enhanced decohesion (HEDE) [16,19] or the localized plasticity (HELP) [20,21] mechanisms. The analysis of the fracture surface after a fracture toughness test can identify the mechanism or mechanisms and support the choice of the most suitable numerical framework. Besides this focus on the active mechanism, the numerical literature based on the Finite Element Method (FEM) reports some strategies to simulate crack advancement and fracture energy degradation in presence of hydrogen, such as the phase field modelling [22,23], the peridynamics [24,25] and the Cohesive Zone Modelling (CZM) [19,26]. This last numerical strategy is suitable when crack propagation is known, as in the case of laboratory toughness tests on standard C(T) specimens.

The second point regards the selection of the inputs for the numerical models. Indeed, a quite complex series of equations [14,27] describes the hydrogen diffusion coupled with the strain analysis, requiring multiple input quantities. Some numerical works accepted literature inputs experimentally obtained for steel grades different from the one object of study due to the few available data. This could lead to numerical results that are imprecise or do not fully match with the specific fracture toughness tests that are being simulated [28]. Hence, focusing on this type of test, it is fundamental to customize the inputs of the numerical models based on the analysed steel. Preliminary experimental tests such as the tensile and the permeation tests allow for estimating mechanical and chemical input quantities, which are at the basis of the numerical models to obtain accurate estimations of hydrogen concentrations, driving the crack tip propagation.

Once the customized framework and inputs are selected based on the steel grade to simulate, the numerical outputs should be compared with the experimental quantities for the validation. Eventually, the numerical models allow estimating hydrogen concentrations in the lattice and the traps, becoming advanced tools to evaluate the effect of hydrogen in loaded components.

This paper focuses on the 2,25Cr1Mo steel grade (ASTM A387 Grade 22 [29]), typically used in high wall pressure reactors, pipelines, etc. In the past, some works studied experimentally the influence of hydrogen on the mechanical properties of this steel [11,30,31]. However, the hydrogen diffusion kinetics through the steel microstructure in terms of trapping effects (i.e. influence of the hydrogen trapping sites) should be better addressed in order to understand the damage at the crack tip. Therefore, the definition of the hydrogen states (diffusible hydrogen and trapped hydrogen) is relevant to discuss the impact of hydrogen on the mechanical properties of the steels [32,33].

The numerical framework developed in [34] can be considered adequate, because it was mainly implemented for medium and high strength steels. Indeed, that framework based on CZM considers the HEDE mechanism but accounts also for the dislocations as the main type of hydrogen trap. It starts from the hydrogen in the lattice and then estimates the hydrogen in the only dislocations, e.g. any other trap is not implemented. The work will not move into the details of the numerical formulation, published in previous papers; rather, we will focus our attention on the importance of a proper selection of the input quantities, performing *ad hoc* preliminary tests to determine the mechanical (elastic modulus, yield stress, ultimate strength) and physical quantities (average hydrogen concentration, diffusion coefficient, dislocation density). Some of these tests were performed by the authors in previous works [6,35,36], recalled in Sect. 2 where the material is presented. Other tests are specifically performed for this study; Sect. 3.1 will describe the methods and Sect. 4.1 the experimental results, which will be used for the numerical simulations.

The work aims to underline the role of these experimental tests to obtain precise and reliable numerical outputs. The comparison between the experimental and the numerical crack tip opening displacement (CTOD) curves, or R-curves, will confirm this customized approach and stress the validity of the model. The discussion of the obtained results will focus on the numerical estimations of the hydrogen concentrations at the crack tip and along the ligament, which can increase the embrittling effect and the crack propagation speed, hence reducing the steel toughness.

2 Material

A low-alloyed ferritic steel from the Cr-Mo family was selected in this study. The chemical composition of the steel, in weight %, is shown in Table 1. It was austenitized at 940 °C for 30 min, quenched in water and finally tempered at 600 °C for 2 h.

Table 1: Chemical composition.

Steel grade	C	Mn	Si	Cr	Mo
2.25Cr1Mo	0.143	0.563	0.157	2.23	1.00

Table 2 shows the Brinell hardness (HB) and the tensile properties (E: elastic modulus, σ_{ys}: yield strength, σ_{uts}: ultimate tensile strength, e: total elongation and J_i: fracture toughness). In the same table, K and n coefficients derived from the Hollomon´s law are also shown, being σ_v the true stress and ε_{pv} the true plastic strain.

Table 2: Mechanical properties.

Steel grade	HB	E (MPa)	σ_{ys} (MPa)	σ_{uts} (MPa)	e (%)	J_i (kJ/m²)	Hollomon´s law: $\sigma_v=K\cdot\varepsilon_{pv}^n$	
							K (MPa)	n
2.25Cr1Mo	285	210000	761	895	21.0	743	1120	0.06

Figure 1 displays the fitting of the Williamson-Hall method, used to determine the dislocation density of the 2,25Cr1Mo steel grade. The analysis methodology was clearly described in [32,36] and it is based on the full width half maximum (FWHM) which is calculated in the different 2Θ(°) positions corresponding to the martensite/ferrite diffraction planes.

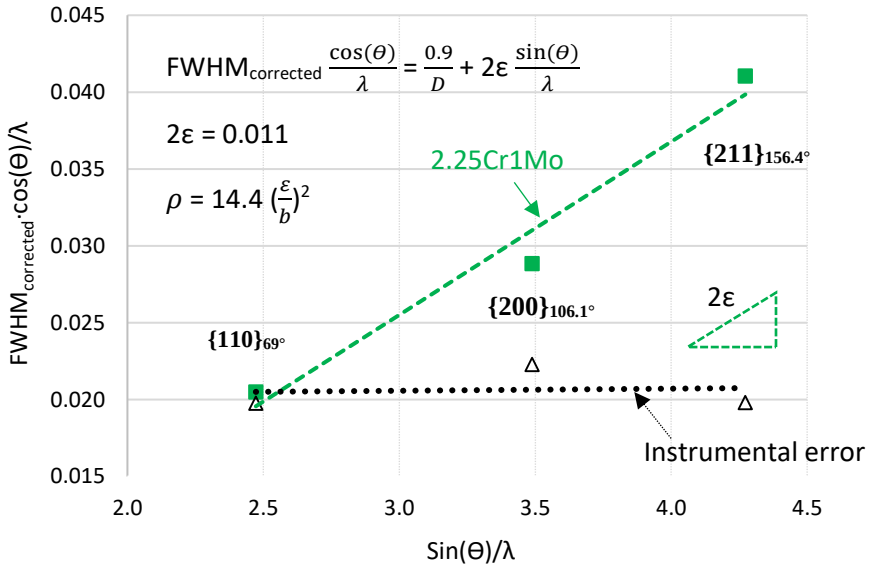

Figure 1: Data fitting to determine the dislocation density

It is worth noting that after the aforementioned heat treatment, the dislocation density was notably high, in the order of $7\cdot10^{15}$ sites/m^2. O. Haiko et al [37] found dislocation densities in the quenched and tempered state in the range of $3\text{-}7\cdot10^{15}$ sites/m^2.

Therefore, dislocations are expected to be the main type of hydrogen trapping site in this study. This hypothesis is also reinforced after studying the interaction between hydrogen atoms and steel microstructure in [36]. Accordingly, the binding energy (E_b) found by TDA analysis was 30 kJ/mol. This energy is associated to the interaction of hydrogen atoms with the elastic field of dislocations [14,38] and it has been considered in this study as a reversible hydrogen trapping site.

On the other hand, fracture toughness results in presence of internal hydrogen are given in Figure 2. C(T) samples were precharged at high temperature in a high pressure hydrogen reactor under the conditions described in Table 3. For more details, the reader is addressed to [6].

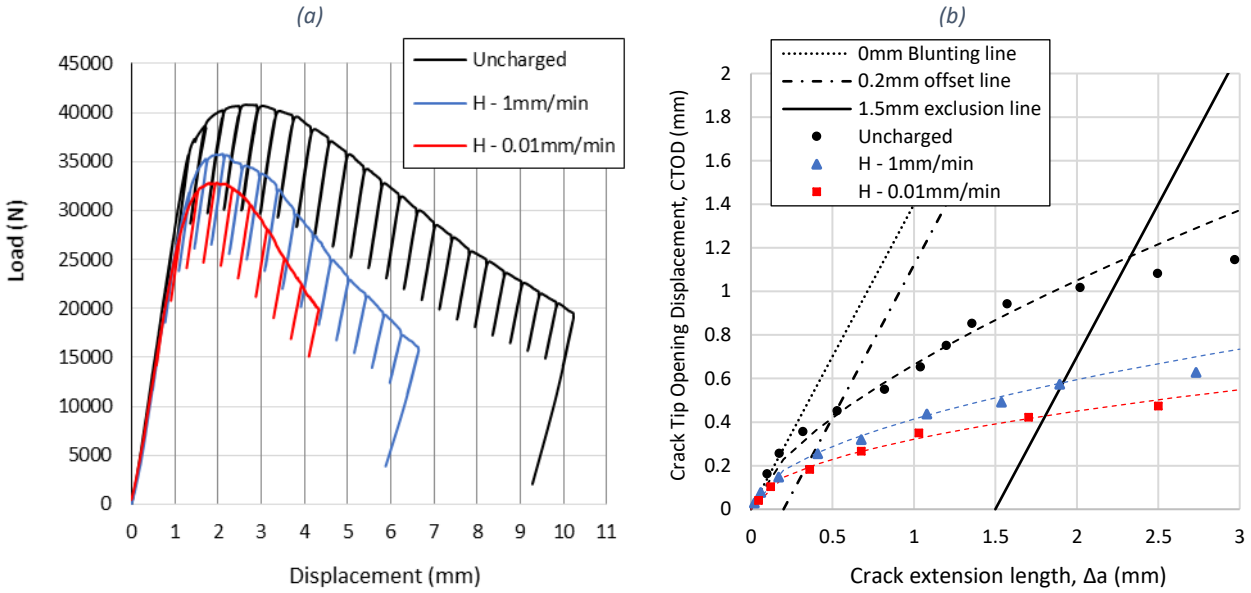

Figure 2: (a) Load-displacement curve and (b) CTOD-R curve with internal hydrogen.

The crack tip opening displacement (CTOD), the embrittlement index (EI), the fracture micromechanisms by order of importance and the time necessary for attaining the $CTOD_{0.2}$ are indicated in Table 4.

Table 3: Hydrogen precharging conditions.

Pressure (MPa)	Temperature (°C)	Time (h)
19.5	450	21

Table 4: Summary of the experimental results from the toughness tests.
**MVC: Microvoid Coalescence, PRHIC: Plasticity Related Hydrogen Induced Cracking and IG: Intergranular fracture.*

Test condition	$CTOD_{0.2}$ (mm)	EI (%) $CTOD_{0.2}$	*Fracture micromechanism	t (s)
Uncharged	0.44	-	MVC	1511
H-1mm/min	0.24	45	MVC + PRHIC + IG	921
H-0.01mm/min	0.18	59	PRHIC + IG + MVC	18840

In order to know the hydrogen concentration introduced into the samples, cylindrical pins (10 mm diameter) were used. Hydrogen content was determined by means of thermal desorption analysis (TDA), using a Leco DH603 hydrogen analyzer. The initial hydrogen content after thermal precharging (C_{H0}) and the final hydrogen content (C_{Hf}) at room temperature were determined. The difference between these two values corresponds to the diffusible hydrogen (C_{Hd}). C_{Hf} is the hydrogen strongly trapped (not contributing to steel embrittlement) in the microstructure whilst, C_{Hd} remains weakly trapped, and it is able to move through the steel microstructure. All the hydrogen values measured in the 2,25Cr1Mo steel grade are given in Table 5.

Table 5: Experimental hydrogen concentrations.

C_{H0} (wppm)	C_{Hf} (wppm)	C_{Hd} (wppm) = lattice + trapped reversibly
1.3	0.6	0.7

However, the numerical analysis considers the only lattice hydrogen content as initial boundary condition. Hence, not all the diffusible hydrogen (0.7 wppm) can be considered for the numerical simulations. Additionally, these hydrogen contents were conducted on cylindrical pins, whose geometry is different from the specimens, and consequently, hydrogen content in C(T) samples can be different. In order to estimate the lattice hydrogen concentration (i.e. interstitial content), electrochemical permeation tests were done. Interstitial hydrogen together with the reversibly trapped in dislocations (E_b~30 kJ/mol) can diffuse towards the crack tip region, which contributes to weakening the steel microstructure.

3 Methods

3.1 Electrochemical Hydrogen Permeation test

Hydrogen diffusion kinetics was analyzed using an electrochemical double cell [32]. Hydrogen was generated on the charging cell under a current density of 1 mA/cm^2, using a 1 mol/l H_2SO_4 + 0.25 g/l of As_2O_3 solution (pH = 1). A circular area of 1 cm^2 was exposed to the solution. The hydrogen exit side contained 0.1 mol/l NaOH solution (pH = 12.5). On the anodic side (hydrogen exit), steel face was electrolytically coated with palladium and then, it was potentiostatically polarized at a constant potential of -50 mV versus a silver/silverchloride (Ag/AgCl) reference electrode during the permeation test. The current density, J(t), on the anodic side (hydrogen flow rate) was continuously recorded using an Ivium PocketSTAT potentiostat.

To estimate the lattice diffusion coefficient ($D_{Lattice}$) and the interstitial content, the discharge phase was used after switching-off the cathodic current on the charging cell. According to Zakroczymski, in the initial part of the discharge curve, desorption of the interstitial hydrogen prevails and this part of the desorption curve is well described by the theoretical Fick´s law [39]. Supposing that the hydrogen subsurface concentration is constant, the diffusion process can be described according to Eq. (1). This equation represents the transport of hydrogen atoms where the steel membrane is supposed to be free of trap sites. If the experimental data adjustment is evaluated in the range where $1 \geq J(t)/J_{max} \geq 0.9$, theoretical lattice diffusivity can be determined by means of Eq. (1) and (2):

$$\frac{J(t)}{J_{max}} = 1 - \frac{2}{\sqrt{\pi \cdot \tau}} \sum_{n=0}^{\infty} \exp\left(-\frac{(2n+1)^2}{4\tau}\right) \quad (1)$$

$$\text{where: } \tau = \frac{D_{Lattice} \cdot t}{L^2} \text{ , if } 1 \geq J/J_{max} \geq 0.9 \quad (2)$$

Here, J(t) is the hydrogen permeation flux depending on the time (t), J_{max} the hydrogen permeation flux at steady-state and L the thickness of the sample (1 mm in this study).

Additionally, the complete decay can be used to quantify the lattice hydrogen content and also the reversible trapped hydrogen [32]. Figure 3 shows as an example, the experimental desorption curve on the exit side.

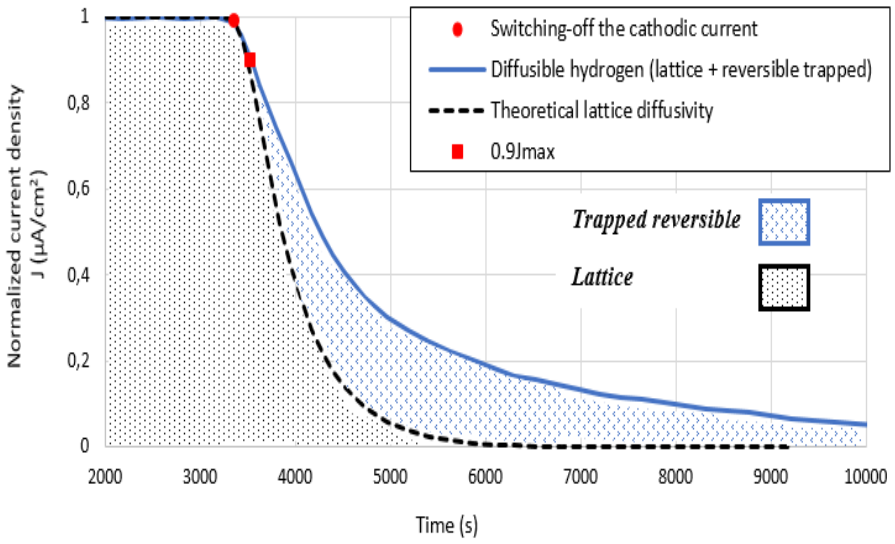

Figure 3: Hydrogen desorption. Image taken from [32].

Accordingly, the area, A, in µA·s/cm^2, defined below the theoretical lattice diffusivity, corresponds to the lattice hydrogen content (C_L). This area can be converted in wppm of hydrogen using the Eq. 3. $D_{Lattice}$ and C_L determined from the electrochemical permeation analysis are taken as an input in the numerical simulations. M_H is the molar mass of hydrogen (1 g/mol), F the Faraday constant (96485 C/mol), L the thickness of the sample and ρ_{Fe} the iron density (7.87·10^6 g/m^3).

$$C_H = A \cdot \frac{M_H}{F \cdot L \cdot \rho_{Fe}} \quad (3)$$

The apparent diffusion coefficient was calculated by Eq. 4 [40],where L is the thickness of the sample and t_{Lag} is the time to attain J=0.63J_{max}, being J the current density and J_{max} the current density corresponding to the steady-state.

$$D_{app} = \frac{L^2}{6 \cdot t_{lag}} \quad (4)$$

3.2 Numerical simulations

The numerical simulations focus on the fracture toughness tests in presence of hydrogen. All the simulations are implemented in Abaqus v.2019 and consider half C(T) specimen, with the simplified rectangular geometry of 48x28.8 mm given in Figure 4.a. Cohesive elements (COH2D4) are placed in correspondence of the ligament, sharing their upper nodes with the adjacent continuum elements, having plane strain formulation (CPE4RT). Their thickness is null at the beginning of the simulation. In order to simulate mode I loading at the crack tip, the applied boundary conditions are the following: i) vertical loading displacement u_y, applied to edge nodes corresponding to the pins; ii) horizontal displacement locked at the pin nodes; iii) vertical symmetry, e.g. vertical displacement pinned, applied to the bottom nodes of the cohesive elements; iv) relative horizontal displacement locked between upper and lower nodes of the cohesive elements, e.g. shear is not allowed. The mesh has a progressive refinement towards the crack tip with linear multi-point constraints, as in [28,34]. The smallest elements have a square shape with 30µm per side. They are placed at the tip region, which is 1 mm high, 3 mm long ahead of the crack tip and 0.6mm long behind the crack tip. According to similar tests on other steels [41,42], when the crack tip reaches 3mm propagation, the load at the pins decreases and the specimen can be considered failed; hence, the simulation is stopped. The mesh consists of 9412 nodes and 7915 elements.

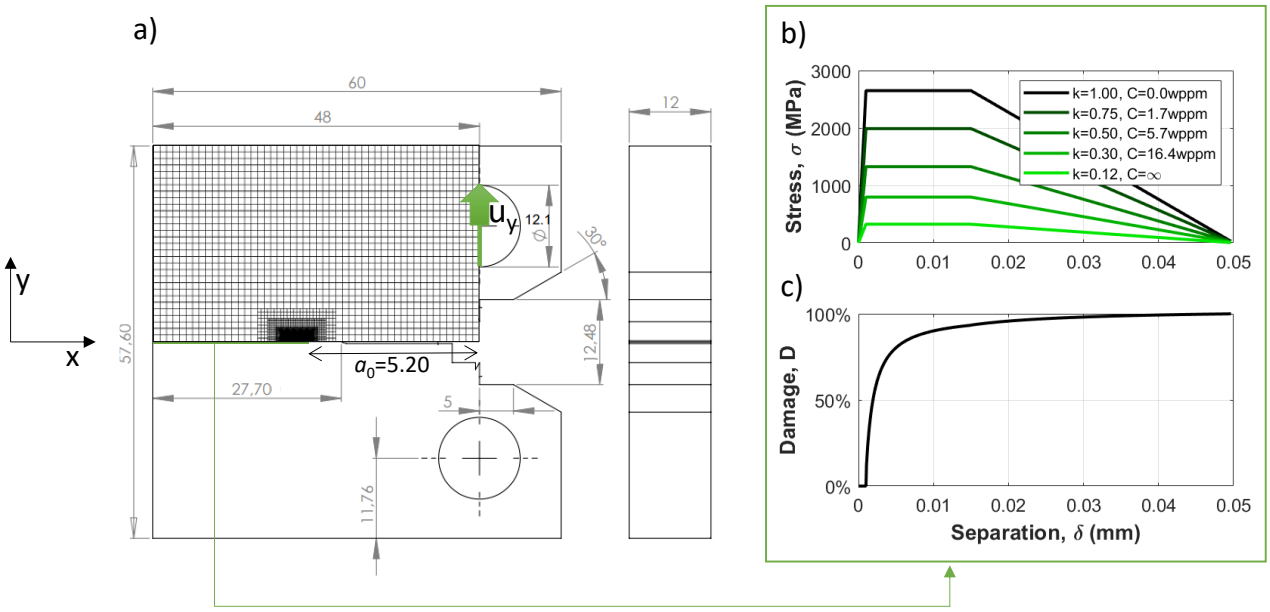

Figure 4: a) Geometry of the C(T) specimen and its geometrical simplification for the numerical simulations, with dimensions in mm; b) calibrated trapezoidal Traction Separation Law – TSL, and c) damage exponential law as a function of the separation.

Two types of simulations are run, with different purposes: 1) without hydrogen; 2) with hydrogen, at different displacement rates. The aim of this first simulation is the calibration of the TSL parameters with trapezoidal shape, e.g. the separations δ_0, δ_1, δ_F, corresponding to the end of the elastic stage, the end of the plateau part, and the final separation of the cohesive element, respectively, and the cohesive strength σ_0. The aim of the second simulations is the estimation of the hydrogen concentrations at the crack tip.

3.2.1 Numerical simulations without hydrogen

The first step of the numerical approach is the simulation of the fracture toughness test without hydrogen pre-charge. The calibration of the TSL parameters is performed with a trial and error procedure to minimize the discrete Fréchet distance [43] between the experimental R curve of the crack tip opening displacement CTOD as a function of the crack growth Δa, and the corresponding numerical one. Table 6 shows the resulting parameters, which will be used also for the next simulations in the presence of hydrogen. They generate the trapezoidal TSL curves of Figure 4.b and the damage curve of Figure 4.c. These TSL plots in presence of hydrogen are function of the decreasing factor k and the total hydrogen concentration C, according to the following equation [44]:

$$k = 1 - 1.0467 \cdot \left(\frac{C}{C + exp(-\Delta g_b^0/RT)}\right) + 0.1687 \cdot \left(\frac{C}{C + exp(-\Delta g_b^0/RT)}\right)^2 \quad (5)$$

where Δg_b^0 is the variation in Gibbs free energy between the microstructural interface and the bulk, equal to 30 kJ/mol, according to the work by Serebrinsky et al [45].

Table 6: Calibrated TSL parameters for the cohesive elements at the ligament.

δ_0 (mm)	δ_1 (mm)	δ_F (mm)	σ_0 (MPa)	σ_0/YS
1.0 E-3	1.5 E-2	5.0 E-2	2650	3.48

3.2.2 Numerical simulations in presence of hydrogen

Two simulations are performed with hydrogen, considering different displacement rates whose R curves are available from the fracture toughness experimental tests, e.g. 1 mm/min and 0.01 mm/min (Figure 2.b). The inputs for these simulations with hydrogen are: i) the experimental data on 2,25Cr1Mo steel available from previous experiments (the mechanical properties in Table 2 and the testing time in Table 4); ii) the cohesive parameters from the numerical calibration without hydrogen (Table 6); iii) the experimental results of the permeation tests (see the diffusion coefficient and hydrogen concentration in the next Sect. 4.1). More in details, we set uniform hydrogen concentration in the lattice $C_{L,0}$ at the beginning of the analysis. It is worth mentioning that the used numerical framework considers as an input only this concentration, updated during the simulations at each integration point. The concentration in the dislocations C_T (the only type of traps considered in the model) is automatically estimated from it, according to Oriani's theory [46,47]:

$$C_T = \frac{N_T K_T C_L}{(K_T - 1)C_L + N_L} \tag{6}$$

where N_L is the density of the interstitial lattice sites equal to $5.1 \cdot 10^{29}$ sites/m^3 [48], and K_T is the equilibrium constant:

$$K_T = exp\frac{E_B}{RT} \tag{7}$$

where R is the universal gas constant and T is the absolute room temperature.
Besides, N_T in Eq. 6 is the density of the trap sites. This is a function of the plastic strain ε_P numerically calculated in each increment and at each integration point, and it follows this formulation:

$$log\, N_T = A - 2.33\, exp(-5.5\varepsilon_p) \tag{8}$$

According with the original exponential formulation proposed by Krom et al [49], the constant A was equal to 23.26, obtained from the fitting of experimental results on α-Fe by Kumnick and Johnson [50]. This corresponds to a traps density in absence of plastic strain ($N_{T,0}$) equal to $8.5 \cdot 10^{20}$ sites/m^3. However, more recent works on other steels [42,51,52] underlined that this value cannot be generalized and needs for a customization based on the tested material. Indeed, Shi et al [53] found 10^{23}-10^{26} sites/m^3 as the typical range of total hydrogen trap density for martensitic steels. However, if we assume only one trapping site, e.g. the dislocations simulated in the numerical framework, this $N_{T,0}$ interval reduces to 10^{23}-10^{25} sites/m^3 according to the experimental works of [50,54].

Among all the mentioned inputs to the numerical model, $N_{T,0}$ specific for dislocations is the only quantity that is difficult to obtain from experimental tests. For this reason, we used this interval of possible values to run a calibration of $N_{T,0}$ with the numerical model. We used the model with displacement rate 1 mm/min and compared the experimental and numerical results in terms of CTOD-Δa curve, similarly to the previous calibration without hydrogen to obtain the TSL parameters. This allowed us to determine the constant A of Eq. 8, resulting equal to 26.37. It corresponds to $N_{T,0}$ equal to $1.1 \cdot 10^{24}$ sites/m^3, e.g. approximately in the middle of the literature interval. Besides, this $N_{T,0}$ is in good agreement with other experimental results [55] and numerical approximations [56] for similar steels, as visible in Figure 5.

The last numerical model with hydrogen at the test speed 0.01 mm/min will allow proving the goodness of the simulation framework. Eventually, both the lattice and the traps concentration fields as a function of time and space are the main outputs of the models.

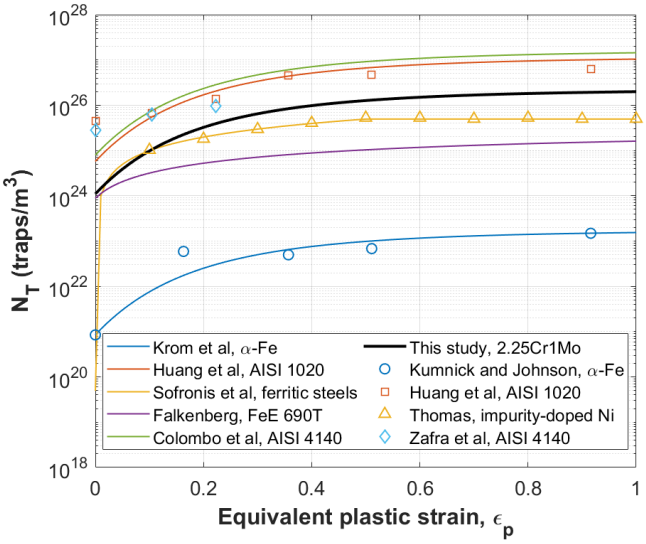

Figure 5: Trap density N_T as a function of the equivalent plastic strain ε_p.
Analytical laws are: Krom et al [49]*, Huang et al* [51]*, Sofronis et al* [57]*, Falkenberg* [56]*, Colombo et al* [42].
Experimental data: Kumnick and Johnson [50]*, Huang et al* [51]*, Thomas* [55]*, Zafra et al* [58].

4 Results

4.1 Electrochemical Hydrogen Permeation test

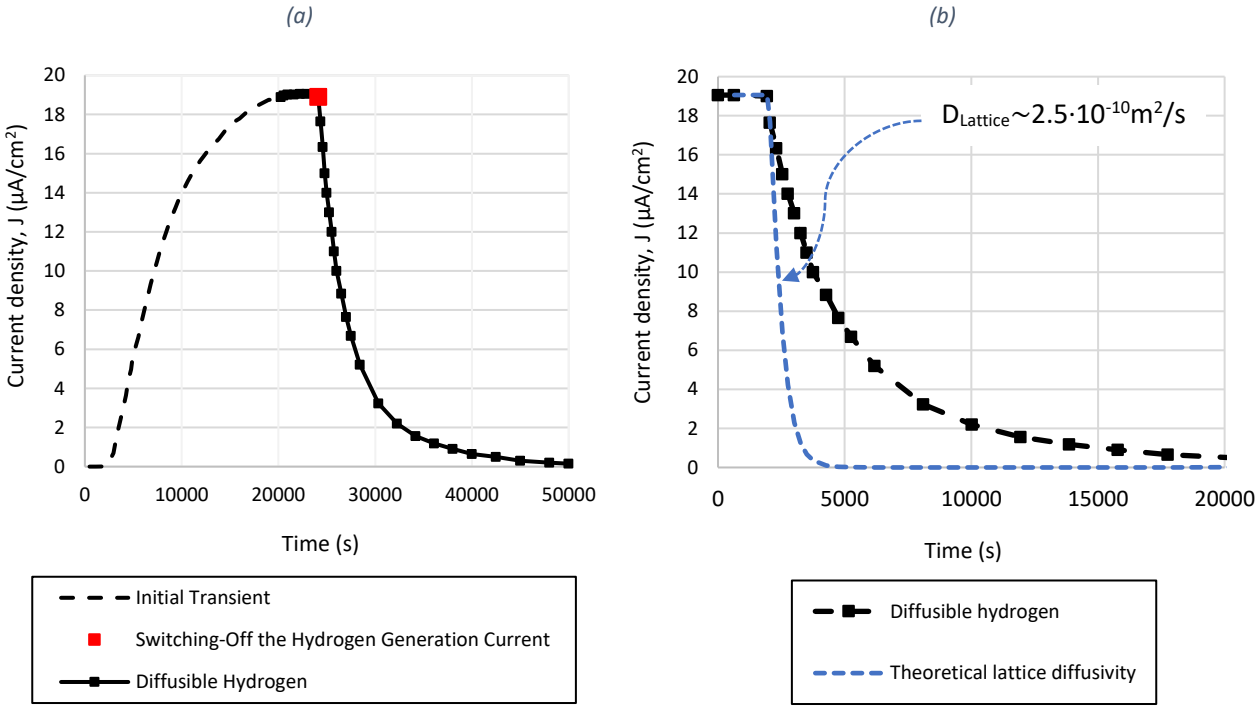

Figure 6: (a) Electrochemical hydrogen permeation curve. (b) Decay transient after switching-off the current of hydrogen generation

Table 7: Parameters used for the simulations with hydrogen.

D_{app} (m^2/s) Eq. 4	$D_{Lattice}$ (m^2/s) Eq. 1	$A_{L,0}$ ($\mu A \cdot s/cm^2$) Figure 3	$C_{L,0}$ (wppm) Eq. 3
$2.1 \cdot 10^{-11}$	$2.5 \cdot 10^{-10}$	12825	0.170

Figure 6.a shows the electrochemical hydrogen permeation curve. Besides, Figure 6.b gives the theoretical data adjustment ($1 \geq J/J_{max} \geq 0.9$) performed to estimate the lattice diffusion coefficient ($D_{Lattice} \sim 2.5 \cdot 10^{-10}$ m^2/s). The area under the theoretical lattice diffusivity curve (12825 $\mu A \cdot s/cm^2$) corresponds to the interstitial content of hydrogen ($C_{L,0}$ = 0.170 wppm, see Table 7). Table 7 summarizes all these quantities, which are used as an input in the numerical model. In particular, it is worth mentioning that, from this $C_{L,0}$ and Eq.6, it is possible to estimate the initial concentration in the dislocations $C_{T,0}$ as 0.055 wppm, and the corresponding initial total hydrogen content C_0 = 0.225 wppm, which is their sum.

4.2 Numerical results

Figure 7 compares three couples of experimental and numerical CTOD-Δa curves (R-curves), which are the curves without hydrogen and the curves with hydrogen at two different test displacement rates. The matching of the curves without hydrogen is used to fit the calibrated TSL parameters. The matching of the curves with hydrogen at 1 mm/min allowed calibrating $N_{T,0}$. On the other hand, the experimental-numerical matching of the curves with hydrogen at 0.01 mm/min represents the validation of the implemented numerical framework and of all the specific input from the experimental tests, supporting its application to the case of the 2,25Cr1Mo steel. This paves the way towards the discussion on the hydrogen concentrations' fields at the crack tip.

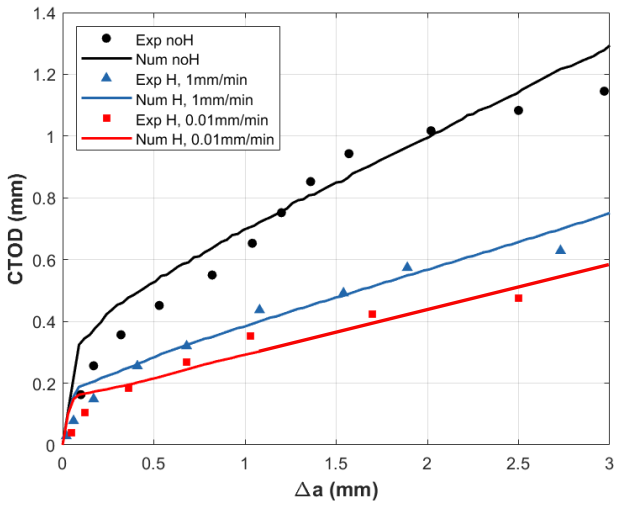

Figure 7: Comparison between the CTOD-Δa curves from experimental tests (Exp) and numerical simulations (Num), without hydrogen (noH) and with hydrogen (H).

Since these results are function both of the space and of the time, the representation becomes three-dimensional. Figure 8 summarizes these three-dimensional trends of the hydrogen C_L, C_T and C concentrations as a function of both the distance from the initial crack tip, e.g. along the ligament, and the percentage time with respect to the total time to reach Δa=3mm. The figure compares these trends for the two models with hydrogen: Figure 8.a,b,c at 1mm/min and Figure 8.d,e,f at 0.01mm/min. In these plots, two vertical lines are plotted. The first one corresponds to the time increment when CTOD=0.01mm, which is twice the δ_F value (because the numerical model considers half the specimen). Hence, this CTOD value defines the time when the numerical model predicts crack initiation. The second vertical line is at the time

when CTOD=0.24mm for 1mm/min and CTOD=0.18mm for 0.01mm/min; they are the experimental values at the 0.2mm offset blunting line. These last CTOD values and their corresponding times are selected to have a hybrid approach, numerical and experimental, for the estimation and analysis of the hydrogen concentrations. Indeed, the definition of the blunting line in the standard [59] assumes that the crack already propagated 0.2mm for the calculation of the main fracture mechanics quantity, the J-integral. Table 8 summarizes the main outputs of the simulations at these CTOD values.

Besides, for the sake of clarity, we can plot in Figure 9.a,b the same concentrations at the first continuum element ahead the initial crack tip, as a function of the CTOD (instead of the time). On the other hand, fixing the time, we can plot the hydrogen concentrations in Figure 10.a,b. The selected time corresponds to the numerical onset of crack propagation, occurring when the first cohesive element at the crack tip is fully damaged with D=100%, meaning that its separation reaches δ_F.

Eventually, Figure 11 gives the concentration fields at 1mm/min, selecting the times corresponding to CTOD=0.10mm and CTOD=0.24mm. Similarly, Figure 12 gives the concentrations' fields at 0.01mm/min, for CTOD=0.10mm and CTOD=0.18mm.

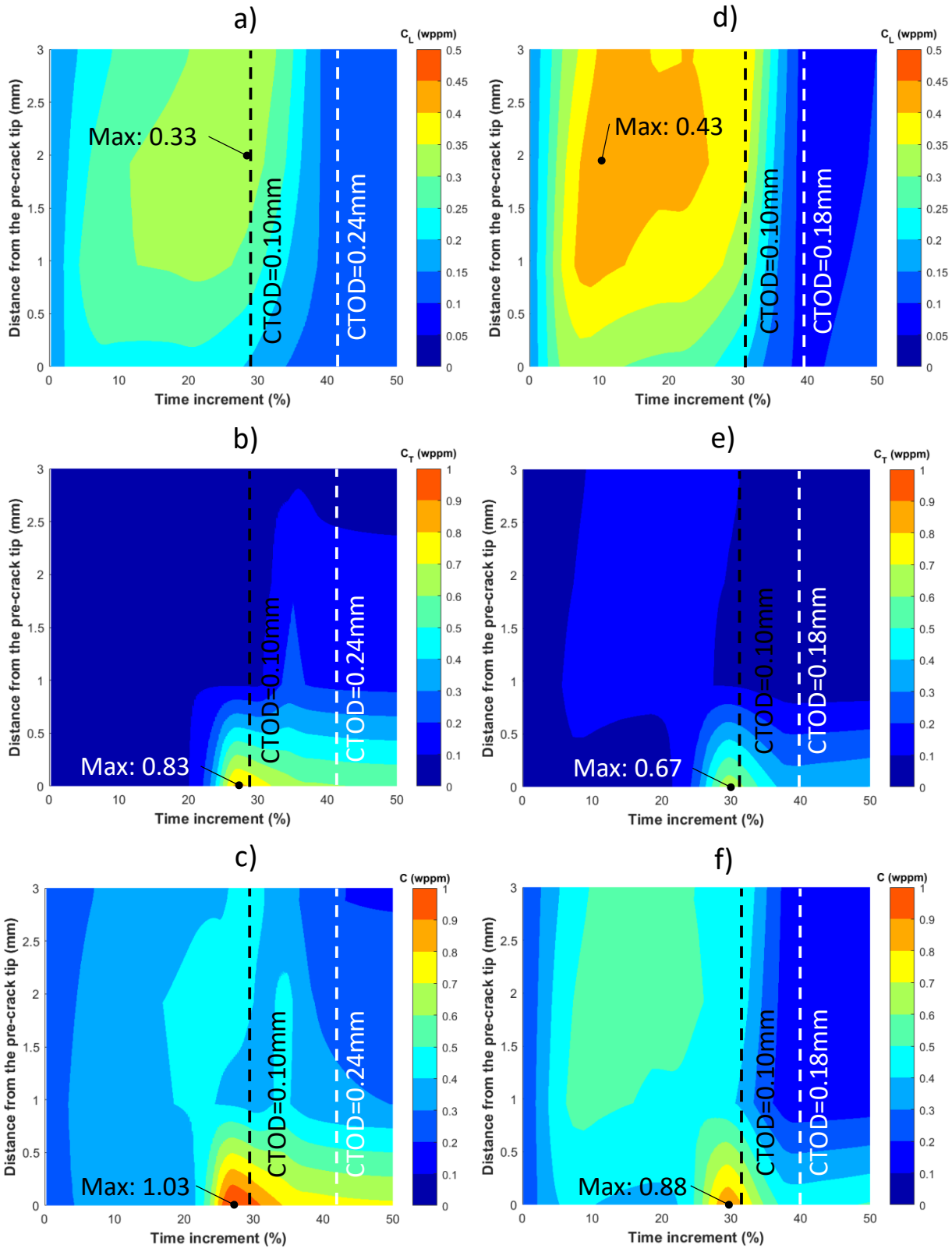

Figure 8: Trends of hydrogen concentrations in lattice C_L, in traps C_T and total C as a function of the distance from the initial crack tip and of the time: a-b-c) 1mm/min; d-e-f) 0.01mm/min.

Table 8: Summary of the main outputs of the simulations at: a) 1mm/min; b) 0.01mm/min.

a)

	CTOD=0.10mm	**CTOD=0.24mm**
Δ*a* (mm)	0.03	0.3
Number of failed cohesive elements	1	10
Time percentage	28.5%	42.2%
C_L at the first element (wppm)	0.195	0.134
C_T at the first element (wppm)	0.799	0.602
C at the first element (wppm)	0.994	0.735

b)

	CTOD=0.10mm	**CTOD=0.18mm**
Δ*a* (mm)	0.03	0.24
Number of failed cohesive elements	1	8
Time percentage	31.7%	39.7%
C_L at the first element (wppm)	0.183	0.098
C_T at the first element (wppm)	0.601	0.369
C at the first element (wppm)	0.784	0.466

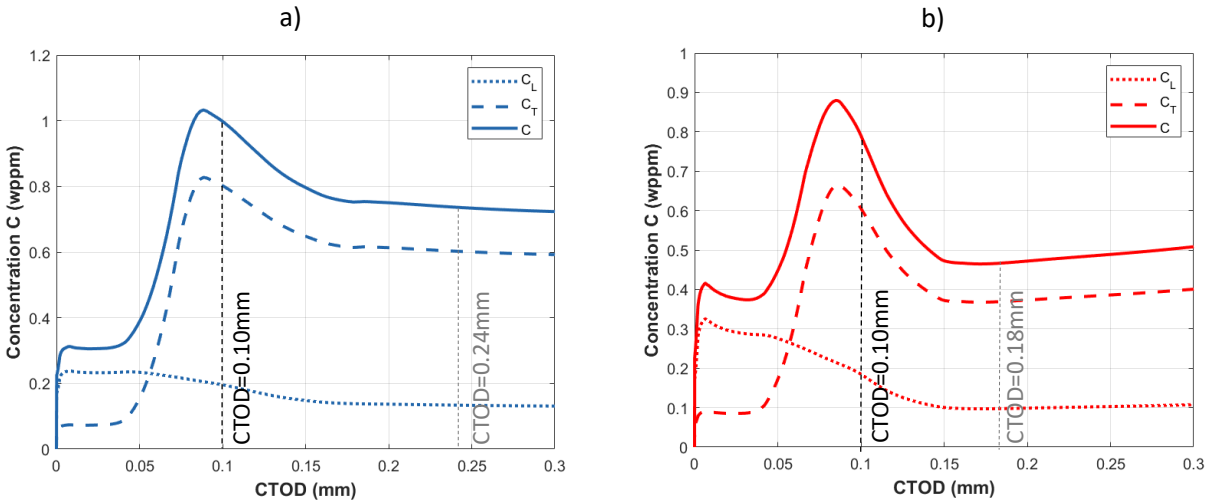

Figure 9: Trends of hydrogen concentrations at the first element ahead the crack tip, as function of the crack tip opening displacement: a) at 1mm/min, b) 0.01mm/min.

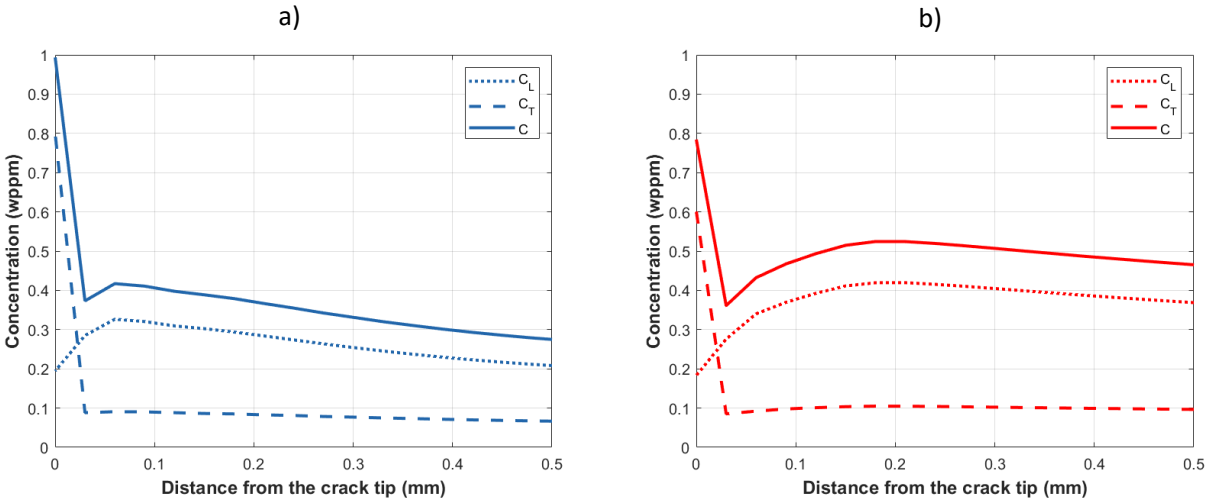

Figure 10: Trends of hydrogen concentration as a function of the distance from the crack tip: a) at 1mm/min, b) 0.01mm/min. The time increment corresponds to the numerical onset of crack propagation, when the first cohesive element at the crack tip is fully damaged.

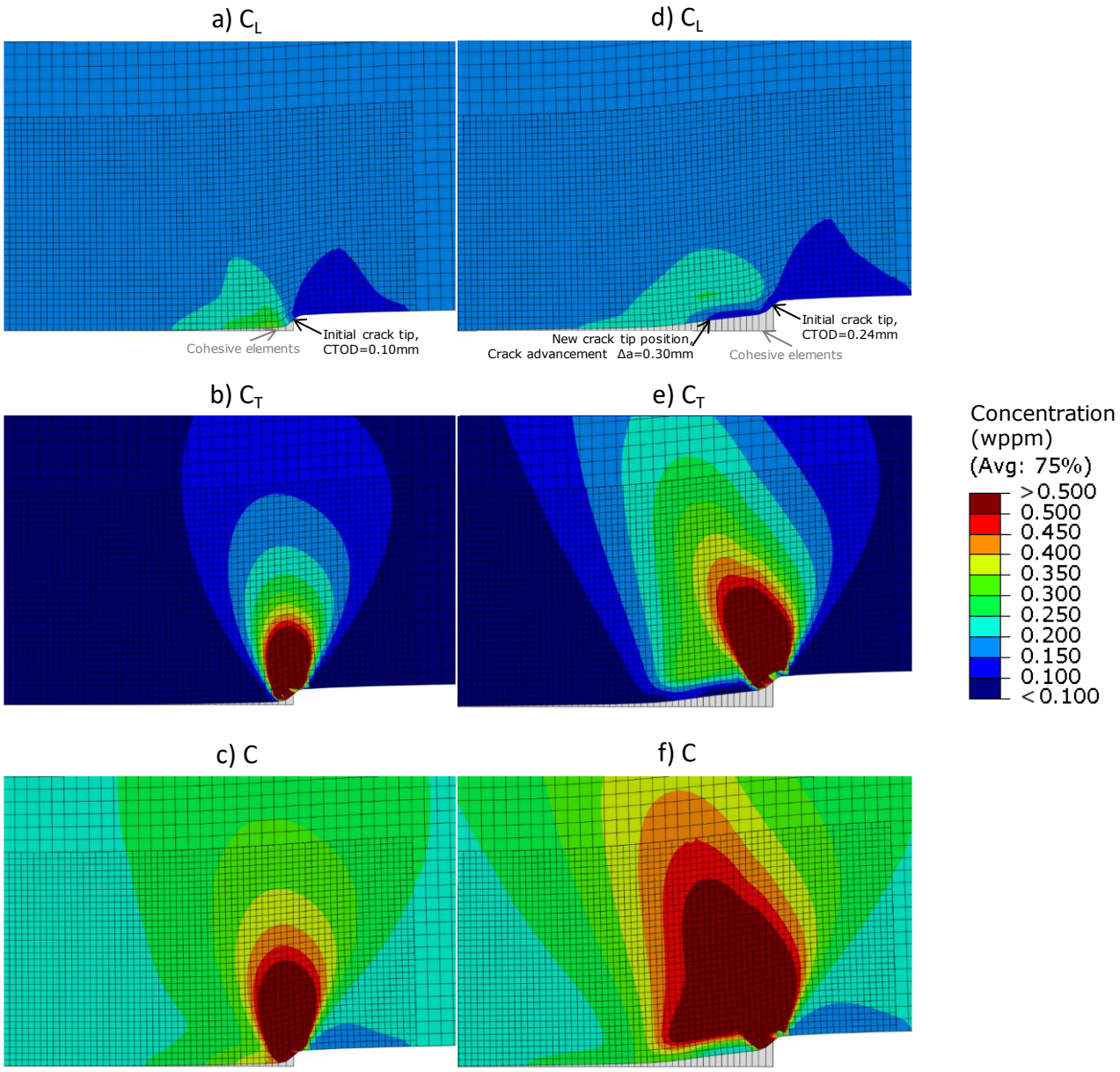

Figure 11: Fields of hydrogen concentrations in lattice C_L, in traps C_T and total C at 1mm/min: a-b-c) CTOD=0.10mm, t=28.5%; d-e-f) CTOD=0.24mm, t=42.2%.

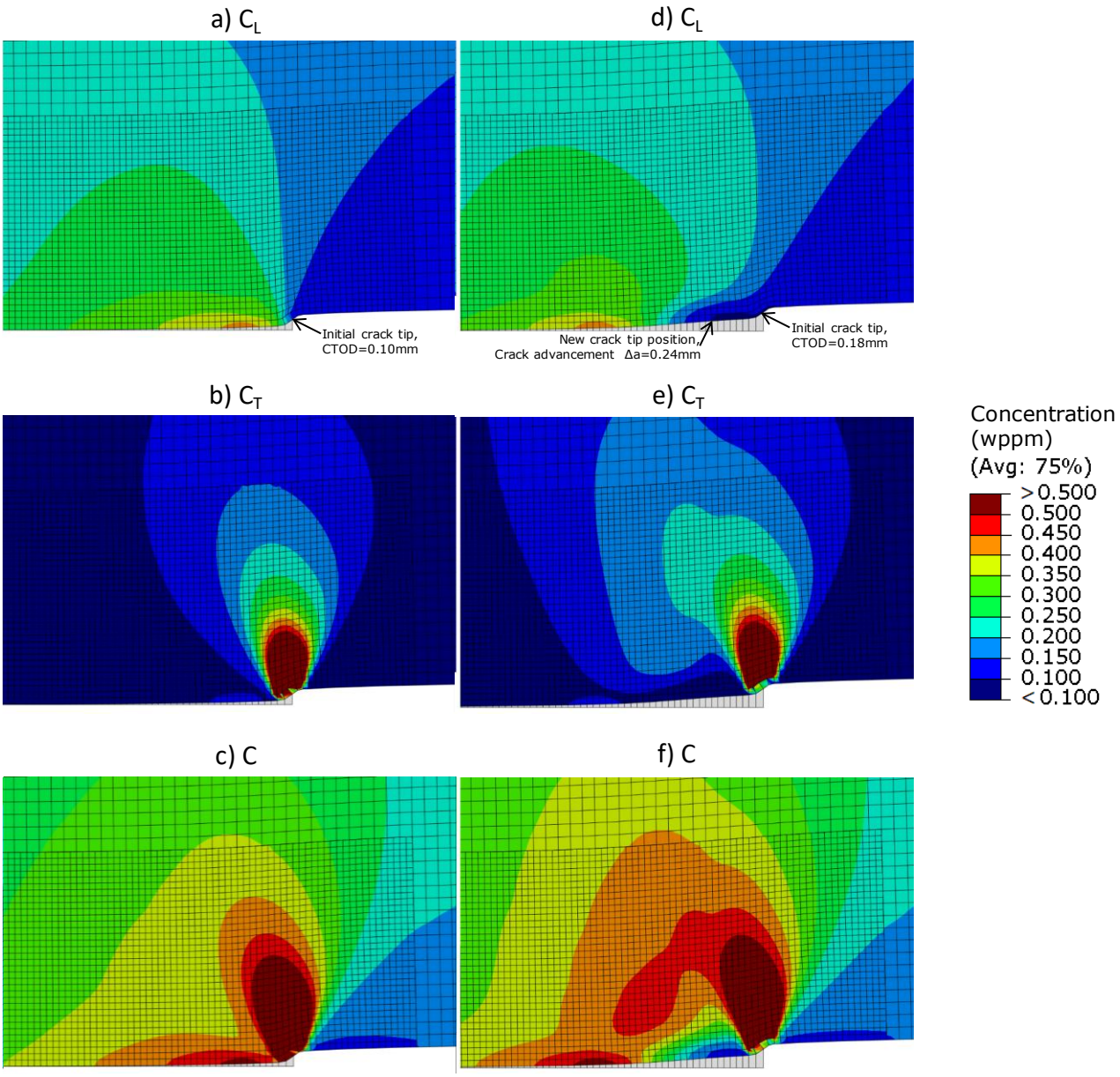

Figure 12: Fields of hydrogen concentrations in lattice C_L, in traps C_T and total C at 0.01mm/min: a-b-c) CTOD=0.10mm, t=31.7%; d-e-f) CTOD=0.18mm, t=39.7%.

5 Discussion

The plots of Figure 8 summarize the hydrogen concentrations at all the continuum elements adjacent to the ligament and starting from the position of the initial crack tip. Let us focus at first on the model implemented at 1mm/min.

Numerically, the crack starts propagating when CTOD=0.1mm=$2\delta_F$, which corresponds to 28.5% of the total simulation time (Table 8.a). This means that about 1/3 of the simulation is spent to cumulate sufficient hydrogen at the initial crack tip, decrease its cohesive strength and reach full damage of the cohesive element. At that time (vertical left grey lines in Figure 8,a,b,c), C_L increases along the cohesive ligament and experiences a maximum ahead of the crack tip where the hydrostatic stress gradient is maximum, see Figure 8.a and Figure 11.a. On the other hand, C_T is mainly concentrated at the initial tip based on the plastic strain field, see Figure 8.b and Figure 11.b. Since C_T is much bigger than C_L, the total hydrogen concentration is

mainly influenced by this concentration in the dislocations, see Figure 8.c and Figure 11.c. After the full damage of the first cohesive element and increasing the simulation time, the accumulation of hydrogen at the new crack tip position is minimal, and the crack advances rapidly, almost independently on the hydrogen concentration. From the plots of Figure 8.a,b,c, it seems that hydrogen plays a major role in the crack initiation rather than in its propagation.

Figure 9.a extracts a 2D plot of the three concentrations along the horizontal axis of Figure 8.a,b,c, e.g. at the distance from the initial crack tip equal to zero. Here it is clearer the hydrogen trend as a function of the CTOD (proportional to the time). The initial linear portion of the trapezoidal TSL up to δ_0 induces a steep raise both for the C_L and C_T, rapidly reaching 0.23 and 0.31 wppm, respectively. Then, due to the selected shape of the TSL, at the plateau of the cohesive stress, these concentrations also experience a flat trend up to δ_1. After this point, corresponding to the last decreasing part of the TSL, C_L starts decreasing with a monotonic trend even beyond CTOD=0.1mm, meaning that the hydrostatic stress gradient is reducing at this region. On the other hand, C_T increases up to the peak of 0.83 wppm, meaning that the plastic strain is still increasing even during the damage of the first cohesive element at the crack tip. However, before reaching CTOD=0.10mm, the decrease of hydrogen concentration in the traps already occurs. This is related to a decrease in the local stress and strain rates at the initial tip, that induces C_T to follow the C_L trend. Eventually, when the hydrostatic stress gradient becomes null at about CTOD=0.17mm, all the concentrations trends flatten and remain approximately constant.

Figure 10.a extracts a 2D plot of the three concentrations along the dashed vertical line at CTOD=0.10mm of Figure 8.a,b,c. Here, freezing the time, it is clearer the hydrogen trend along the ligament. This is the typical plot extracted from the numerical simulations proposed in other literature papers [41,42,49]. C_L profile experiences a peak at 0.06 mm ahead of the crack tip, i.e. two elements' length; it reflects the hydrostatic stress peak resulting from the stress fields. The plot of Figure 10.a also evidences the peak of the C_T profile at the crack tip, reflecting the high plastic strain in this region. Considering that C is the sum of C_L and C_T, we can state that C_T influences this trend very near to the crack tip, at the very first element, while C_L drives the trend beyond 0.03mm along the rest of the ligament. It is also worth noting that hydrogen cumulates at the crack tip reaching 0.994 wppm (see Table 8), that is 4.42 times the initial total hydrogen concentration C_0.

Together with the results at CTOD=0.10mm, Figure 9-10 also give an overview of the change in concentrations' values and shape of their fields also at CTOD=0.24mm. The simulation reaches this CTOD value when t=42.2%, corresponding to 10 cohesive elements failed and to 0.3mm crack advancement (see Table 8.a). Here the concentrations are lower than for t=28.5%, not only at the new position of the crack tip but anywhere along the ligament. Up to the numerical failure of the first cohesive element, the concentrations increase locally following the stress fields, and, in particular, C_T assumes the typical oval shape reflected into the total C. However, following the crack propagation sequence up to Δa=0.3mm, the total concentration field changes its shape and follows the tip, mainly driven by the C_L concentration (see Figure 11.d,e,f). Indeed, almost no further increase in plastic strain occurs, and C_T field remains frozen.

According to these results on the 2,25Cr1Mo steel, we can state that the experimental estimation of J-integral, which is based on the 0.2mm offset of the blunting line, implies that the new position of the crack tip, already propagated, is mainly affected by the concentration in the lattice. In other words, the hydrogen concentration in the traps (dislocations) plays a major role in the initiation, e.g. at the initial position of the crack tip, while the hydrogen concentration in the lattice enhances the propagation at this testing speed.

Let us now focus on the second numerical model with hydrogen, implemented at 0.01mm/min. Here, the crack starts propagating at 31.7% of the total simulation time (Table 8.b), which is quite similar to the case at 1mm/min. However, the difference lays in the concentrations at the tip. Indeed, from Figure 8.d,e,f we can state that the C_L concentration along the ligament is quite different with respect to the previous displacement rate, 1mm/min. In particular, higher C_L values are reached before the failure of the first

cohesive element, because of the longer time for hydrogen diffusion. This feature is visible more in detail in Figure 9.b; C_L experiences a much higher value at the initial crack tip as a function of the CTOD, especially during the initial stage. As a consequence of C_L increasing, C_T decreases because these concentrations follow the local equilibrium theory by Oriani [46,47]. This results in a lower C when the crack starts propagating, e.g. 0.784 wppm (see Table 8.b), that is 3.48 times the initial total hydrogen concentration C_0. This means that the two orders of magnitude decrease in test speed reduces the critical hydrogen concentration of -21%.

Despite the total hydrogen concentration at the initial crack tip is lower at 0.01mm/min than at 1mm/min (see Figure 9.a vs Figure 9.b, or Figure 10.a vs Figure 10.b), this is not the only important quantity to estimate the embrittling effect. Indeed, also the total concentration ahead of the tip, e.g. along the ligament, and the position of its peak play a role. Comparing Figure 11.c vs Figure 12.c, it is clear that the ligament ahead the initial tip position recalls more hydrogen at 0.01mm/min than at 1mm/min, and this causes the crack to propagate very rapidly. In other words, the crack propagation is strongly governed by the stress-strain field around and ahead of the crack tip. By virtue of the hydrogen apparent diffusion coefficient ($D_{app}=2.1\cdot10^{-11}$ m^2/s, see Table 7) and for the lowest displacement rate, hydrogen atoms have more time to diffuse in and out of the crack tip area. Therefore, the lattice hydrogen and the reversible hydrogen trapped in dislocations seem to notably redistribute along the ligament (Figure 12), contributing to activating the embrittlement mechanisms (HEDE, see Figure 13.b) when a critical hydrogen concentration is reached. Accordingly, hydrogen redistribution promoted important changes on the fracture surfaces. Fracture micromechanism changed from ductile (in the absence of hydrogen) to intermediate (martensite lath decohesion, MLD, also known as PRHIC micromechanism) and brittle (IG) in presence of internal hydrogen (Figure 13.b). This fact justifies the biggest drop in the CTOD-R curve (Figure 7) noticed at 0.01 mm/min.

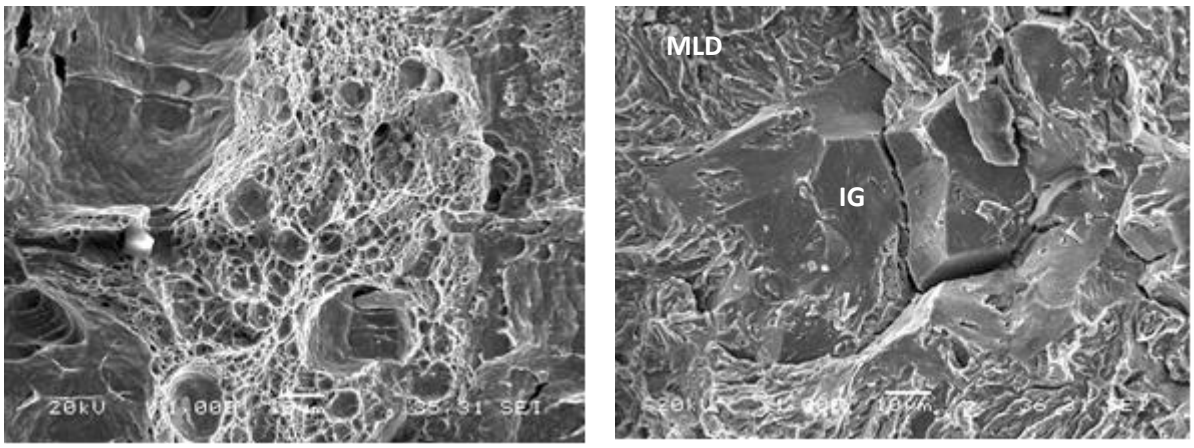

(a) (b)

Figure 13: (a) Uncharged sample: MVC (ductile) (b) Hydrogen precharged sample, tested at 0.01 mm/min: IG fracture and MLD micromechanism.

The different concentration field at the ligament induces the experimental 0.2/BL CTOD to drop from 0.24mm at 1mm/min to 0.18mm at 0.01mm/min. Indeed, when the crack propagates, the crack growth rate is so high that the hydrogen has almost no time to diffuse again towards the new tip and the hydrogen already present along the ligament accelerates the cracking, lowering the CTOD-Δ*a* curve and reducing the corresponding toughness.

6 Conclusions

The work presented the results of a combined experimental and numerical study on CrMo steel, focusing on the effect of hydrogen embrittlement on fracture toughness. *Ad hoc* experimental tests have been performed to collect all the inputs for the numerical model and for the comparison with the numerical outputs, allowing for validation. In particular, the three targeted experimental tests are:

- tensile tests without hydrogen, to obtain the mechanical properties;
- permeation tests, to obtain the diffusion coefficient and the interstitial content of hydrogen;
- fracture toughness tests, to obtain the CTOD-Δa curves without and with hydrogen and to evidence the active embrittling mechanism, which in this case was the HEDE.

Once all these inputs are experimentally obtained, they allow for a specific numerical simulation of the embrittlement both from the mechanical viewpoint in terms of CTOD-Δa curves as well as from the concentrations viewpoint. These last quantities cannot be experimentally measured, and only such a calibrated and accurate numerical tool is able to provide valid estimations. Besides, it allows following the hydrogen redistribution in the lattice and the reversible traps along the ligament, during the initiation and the propagation, promoting changes to the fracture surfaces. In the case of the analysed CrMo steel, we could quantify that the decrease of two orders of magnitude in the test speed reduces the critical hydrogen concentration, activating crack propagation, from 0.994 to 0.784 wppm, e.g. -21%. Despite the complexity of the numerical framework and the multiple inputs required from these targeted experimental tests, this tool could be extremely useful for the design purposes of steel components operating in presence of hydrogen, because it allows estimating a critical concentration, especially as a function of the loading time.

References

[1] Popov BN, Lee JW, Djukic MB. Hydrogen permeation and hydrogen-induced cracking. In: Kutz M, editor. Handb. Environ. Degrad. Mater. Third, Elsevier; 2018, p. 133–62. doi:10.1016/B978-0-323-52472-8.00007-1.

[2] Dwivedi SK, Vishwakarma M. Hydrogen embrittlement in different materials: A review. Int J Hydrogen Energy 2018;43:21603–16. doi:10.1016/j.ijhydene.2018.09.201.

[3] Dadfarnia M, Nagao A, Wang S, Martin ML, Somerday BP, Sofronis P. Recent advances on hydrogen embrittlement of structural materials. Int J Fract 2015;196:223–43. doi:10.1007/s10704-015-0068-4.

[4] Gangloff RP, Somerday BP. Gaseous Hydrogen Embrittlement of Materials in Energy Technologies: Mechanisms, Modelling and Future Developments. Gaseous Hydrog Embrittlement Mater Energy Technol Mech Model Futur Dev 2012:1–500. doi:10.1533/9780857095374.

[5] Laliberté-Riverin S, Brochu M. A novel approach for quantifying hydrogen embrittlement using side-grooved CT samples. Eng Fract Mech 2022;265. doi:10.1016/j.engfracmech.2022.108324.

[6] Peral LB, Zafra A, Belzunce J, Rodríguez C. Effects of hydrogen on the fracture toughness of CrMo and CrMoV steels quenched and tempered at different temperatures. Int J Hydrogen Energy 2019;44:3953–65. doi:10.1016/j.ijhydene.2018.12.084.

[7] Zafra A, Álvarez G, Belzunce J, Alegre JM, Rodríguez C. Fracture toughness of coarse-grain heat affected zone of quenched and tempered CrMo steels with internal hydrogen: Fracture micromechanisms. Eng Fract Mech 2021;241. doi:10.1016/j.engfracmech.2020.107433.

[8] de Assis KS, Lage MA, Guttemberg G, dos Santos FP, Mattos OR. Influence of hydrogen on plasticity around the crack tip in high strength steels. Eng Fract Mech 2017;176:116–25. doi:10.1016/j.engfracmech.2017.02.028.

[9] Sun Z, Benoit G, Moriconi C, Hamon F, Halm D, Hamon F, et al. Fatigue crack propagation under gaseous hydrogen in a precipitation- hardened martensitic stainless steel. Int J Hydrogen Energy 2011;36:8641–4. doi:10.1016/j.ijhydene.2011.04.094.

[10] Murakami Y, Matsuoka S. Effect of hydrogen on fatigue crack growth of metals. Eng Fract Mech 2010;77:1926–40. doi:10.1016/j.engfracmech.2010.04.012.

[11] Colombo C, Fumagalli G, Bolzoni F, Gobbi G, Vergani L. Fatigue behavior of hydrogen pre-charged low alloy Cr-Mo steel. Int J Fatigue 2015;83:2–9. doi:10.1016/j.ijfatigue.2015.06.002.

[12] Alvaro A, Wan D, Olden V, Barnoush A. Hydrogen enhanced fatigue crack growth rates in a ferritic Fe-3 wt%Si alloy and a X70 pipeline steel. Eng Fract Mech 2019;219. doi:10.1016/j.engfracmech.2019.106641.

[13] Shinko T, Halm D, Benoit G, Hénaff G. Controlling factors and mechanisms of fatigue crack growth influenced by high pressure of gaseous hydrogen in a commercially pure iron. Theor Appl Fract Mech 2021;112. doi:10.1016/j.tafmec.2020.102885.

[14] Jemblie L, Olden V, Akselsen OM. A coupled diffusion and cohesive zone modelling approach for numerically assessing hydrogen embrittlement of steel structures. Int J Hydrogen Energy 2017;42:11980–95. doi:10.1016/j.ijhydene.2017.02.211.

[15] Das T, Legrand E, Brahimi S V., Song J, Yue S. Evaluation of material susceptibility to hydrogen embrittlement (HE): An approach based on experimental and finite element (FE) analyses. Eng Fract Mech 2020;224. doi:10.1016/j.engfracmech.2019.106714.

[16] Moriconi C, Hénaff G, Halm D. Cohesive zone modeling of fatigue crack propagation assisted by gaseous hydrogen in metals. Int J Fatigue 2014;68:56–66. doi:10.1016/j.ijfatigue.2014.06.007.

[17] Díaz A, Alegre JM, Cuesta II. Numerical simulation of hydrogen embrittlement and local triaxiality effects in notched specimens. Theor Appl Fract Mech 2017;90:294–302. doi:10.1016/j.tafmec.2017.06.017.

[18] Zhu X, Li W, Hsu TY, Zhou S, Wang L, Jin X. Improved resistance to hydrogen embrittlement in a high-strength steel by quenching-partitioning-tempering treatment. Scr Mater 2015;97:21–4. doi:10.1016/j.scriptamat.2014.10.030.

[19] Olden V, Thaulow C, Johnsen R, Østby E. Cohesive zone modeling of hydrogen-induced stress cracking in 25% Cr duplex stainless steel. Scr Mater 2007;57:615–8. doi:10.1016/j.scriptamat.2007.06.006.

[20] Brocks W, Falkenberg R, Scheider I. Coupling aspects in the simulation of hydrogen-induced stresscorrosion cracking. Procedia IUTAM 2012;3:11–24. doi:10.1016/j.piutam.2012.03.002.

[21] Huang S, Zhang Y, Yang C, Hu H. Fracture strain model for hydrogen embrittlement based on hydrogen enhanced localized plasticity mechanism. Int J Hydrogen Energy 2020;45:25541–54. doi:10.1016/j.ijhydene.2020.06.271.

[22] Martínez-Pañeda E, Golahmar A, Niordson CF. A phase field formulation for hydrogen assisted cracking. Comput Methods Appl Mech Eng 2018;342:742–61. doi:10.1016/j.cma.2018.07.021.

[23] Golahmar A, Kristensen PK, Niordson CF, Martínez-Pañeda E. A phase field model for hydrogen-assisted fatigue. Int J Fatigue 2022;154. doi:10.1016/j.ijfatigue.2021.106521.

[24] Ran X, Qian S, Zhou J, Xu Z. Crack propagation analysis of hydrogen embrittlement based on peridynamics. Int J Hydrogen Energy 2022;47:9045–57. doi:10.1016/j.ijhydene.2021.11.173.

[25] De Meo D, Diyaroglu C, Zhu N, Oterkus E, Siddiq MA. Modelling of stress-corrosion cracking by using peridynamics. Int J Hydrogen Energy 2016;41:6593–609. doi:10.1016/j.ijhydene.2016.02.154.

[26] Fernández-Sousa R, Betegón C, Martínez-Pañeda E. Cohesive zone modelling of hydrogen assisted fatigue crack growth: The role of trapping. Int J Fatigue 2022;162:106935. doi:10.1016/j.ijfatigue.2022.106935.

[27] Díaz A, Alegre JM, Cuesta II. A review on diffusion modelling in hydrogen related failures of metals. Eng Fail Anal 2016;66:577–95. doi:10.1016/j.engfailanal.2016.05.019.

[28] Gobbi G, Colombo C, Miccoli S, Vergani L. A weakly coupled implementation of hydrogen embrittlement in FE analysis. Finite Elem Anal Des 2018;141. doi:10.1016/j.finel.2017.11.010.

[29] ASTM International. ASTM A387/387M-17a: Standard Specification for Pressure Vessel Plates, Alloy Steel, Chromium-Molybdenum 2017:1–6. doi:10.1520/A0387_A0387M-17A.

[30] Peral LB, Zafra A, Blasón S, Rodríguez C, Belzunce J. Effect of hydrogen on the fatigue crack growth rate of quenched and tempered CrMo and CrMoV steels. Int J Fatigue 2019;120:201–14. doi:10.1016/j.ijfatigue.2018.11.015.

[31] Pillot S, Coudreuse L. Hydrogen-induced disbonding and embrittlement of steels used in petrochemical refining. Gaseous Hydrog Embrittlement Mater Energy Technol Probl Its Characterisation Eff Part Alloy Classes 2012:51–93. doi:10.1533/9780857093899.1.51.

[32] Peral LB, Amghouz Z, Colombo C, Fernández-Pariente I. Evaluation of hydrogen trapping and diffusion in two cold worked CrMo(V) steel grades by means of the electrochemical hydrogen permeation technique. Theor Appl Fract Mech 2020;110. doi:10.1016/j.tafmec.2020.102771.

[33] Oudriss A, Fleurentin A, Courlit G, Conforto E, Berziou C, Rébéré C, et al. Consequence of the diffusive hydrogen contents on tensile properties of martensitic steel during the desorption at room temperature. Mater Sci Eng A 2014;598:420–8. doi:10.1016/j.msea.2014.01.039.

[34] Gobbi G, Colombo C, Miccoli S, Vergani L. A fully coupled implementation of hydrogen embrittlement in FE analysis. Adv Eng Softw 2019;135. doi:10.1016/j.advengsoft.2019.04.004.

[35] Peral LB, Fernández-Pariente I, Colombo C, Rodríguez C, Belzunce J. The positive role of nanometric molybdenum–vanadium carbides in mitigating hydrogen embrittlement in structural steels. Materials (Basel) 2021;14. doi:10.3390/ma14237269.

[36] Peral LB, Zafra A, Fernández-Pariente I, Rodríguez C, Belzunce J. Effect of internal hydrogen on the tensile properties of different CrMo(V) steel grades: Influence of vanadium addition on hydrogen trapping and diffusion. Int J Hydrogen Energy 2020;45:22054–79. doi:10.1016/j.ijhydene.2020.05.228.

[37] Haiko O, Kaijalainen A, Pallaspuro S, Hannula J, Porter D, Liimatainen T, et al. The effect of tempering on the microstructure and mechanical properties of a novel 0.4C press-hardening steel. Appl Sci 2019;9. doi:10.3390/app9204231.

[38] Maroef I, Olson DL, Eberhart M, Edwards GR. Hydrogen trapping in ferritic steel weld metal. Int Mater Rev 2003;47:191–223. doi:10.1179/095066002225006548.

[39] Zakroczymski T. Adaptation of the electrochemical permeation technique for studying entry, transport and trapping of hydrogen in metals. Electrochim Acta 2006;51:2261–6. doi:10.1016/j.electacta.2005.02.151.

[40] ASTM International. ASTM G148-97: Standard Practice for Evaluation of Hydrogen Uptake, Permeation and Transport in Metals by an Electrochemical Technique 2018:1–10. doi:10.1520/G0148-97R11.2.

[41] Gobbi G, Colombo C, Vergani L. Sensitivity analysis of a 2D cohesive model for hydrogen embrittlement of AISI 4130. Eng Fract Mech 2016;167. doi:10.1016/j.engfracmech.2016.03.045.

[42] Colombo C, Zafra García A, Belzunce J, Fernandez Pariente I. Sensitivity to hydrogen embrittlement of AISI 4140 steel: A numerical study on fracture toughness. Theor Appl Fract Mech 2020;110. doi:10.1016/j.tafmec.2020.102810.

[43] Danziger Z. Discrete Frechet Distance. MATLAB Cent File Exch 2022.

[44] Hondros ED, Seah MP. Theory of Grain Boundary Segregation in Terms of Surface Adsorption Analogues. Met Trans A 1977;8 A:1363–71. doi:10.1007/BF02642850.

[45] Serebrinsky S, Carter EA, Ortiz M. A quantum-mechanically informed continuum model of hydrogen embrittlement. J Mech Phys Solids 2004;52:2403–30. doi:10.1016/j.jmps.2004.02.010.

[46] Oriani RA. A Mechanistic Theory of Hydrogen Embrittlement of Steels. Berichte der Bunsen-Gesellschaft fur Phys. Chemie, vol. 76, 1972, p. 848–57.

[47] Oriani RA. The diffusion and trapping of hydrogen in steel. Acta Metall 1970;18:147–57. doi:10.1016/0001-6160(70)90078-7.

[48] Sofronis P, McMeeking RM. Numerical analysis of hydrogen transport near a blunting crack tip. J Mech Phys Solids 1989;37:317–50. doi:10.1016/0022-5096(89)90002-1.

[49] Krom AHM, Koers RWJ, Bakker A. Hydrogen transport near a blunting crack tip. J Mech Phys Solids 1999;47:971–92. doi:10.1016/S0022-5096(98)00064-7.

[50] Kumnick AJ, Johnson HH. Deep trapping states for hydrogen in deformed iron. Acta Metall 1980;28:33–9. doi:10.1016/0001-6160(80)90038-3.

[51] Huang H, Shaw WJD. Hydrogen embrittlement interactions in cold-worked steel. Corrosion 1995;51:30–6. doi:10.5006/1.3293573.

[52] Wang Y, Wu X, Zhou Z, Li X. Numerical analysis of hydrogen transport into a steel after shot peening. Results Phys 2018;11:5–16. doi:10.1016/j.rinp.2018.08.030.

[53] Shi R, Chen L, Wang Z, Yang XS, Qiao L, Pang X. Quantitative investigation on deep hydrogen trapping in tempered martensitic steel. J Alloys Compd 2021;854. doi:10.1016/j.jallcom.2020.157218.

[54] Frappart S, Feaugas X, Creus J, Thebault F, Delattre L, Marchebois H. Study of the hydrogen diffusion and segregation into FeCMo martensitic HSLA steel using electrochemical permeation test. J Phys Chem Solids 2010;71:1467–79. doi:10.1016/j.jpcs.2010.07.017.

[55] Thomas GJ. Hydrogen Trapping in FCC Metals. In: Sandia National Labs., editor. No. SAND-80-8656; CONF-800850-3, Livermore, CA (USA): 1981, p. 77–85.

[56] Falkenberg R. Simulation von Wasserstofftransport und Rißwachstum infolge wasserstoffinduzierter Spannungsrißkorrosion mit einer Analyse der Kopplungsphanomenologie (in German). Christian-Albrechts-Universitat, Kiel, 2010.

[57] Sofronis P, Liang Y, Aravas N. Hydrogen induced shear localization of the plastic flow in metals and alloys. Eur J Mech A/Solids 2001;20:857–72. doi:10.1016/S0997-7538(01)01179-2.

[58] Zafra A, Belzunce J, Rodríguez C. Hydrogen diffusion and trapping in 42CrMo4 quenched and tempered steel: Influence of quenching temperature and plastic deformation. Mater Chem Phys 2020:123599. doi:10.1016/j.matchemphys.2020.123599.

[59] ASTM International. ASTM E1820−20b: Standard Test Method for Measurement of Fracture Toughness 2020:1–65. doi:10.1520/E1820-20B.